

Spectroscopic Investigation of the Primary Reaction Intermediates in the Oxidation of Levitated Droplets of Energetic Ionic Liquids

Stephen J. Brotton,[†] Michael Lucas,[†] Steven D. Chambreau,[‡] Ghanshyam L. Vaghjiani,[§] Jiang Yu,^{||} Scott L. Anderson,^{||} and Ralf I. Kaiser^{*,†,||}

[†]Department of Chemistry, University of Hawaii at Manoa, Honolulu, Hawaii 96822, United States

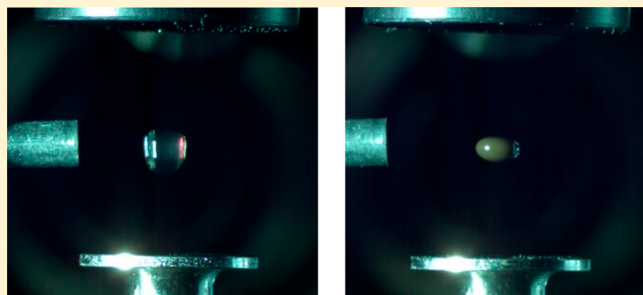
[‡]ERC Inc., Edwards Air Force Base, California 93524, United States

[§]In-Space Propulsion Branch, Rocket Propulsion Division, Aerospace Systems Directorate, Air Force Research Laboratory, AFRL/RQRS, Edwards Air Force Base, California 93524, United States

^{||}Department of Chemistry, University of Utah, Salt Lake City, Utah 84112, United States

Supporting Information

ABSTRACT: The production of the next generation of hypergolic, ionic-liquid-based fuels requires an understanding of the reaction mechanisms between the ionic liquid and oxidizer. We probed reactions between a levitated droplet of 1-methyl-4-amino-1,2,4-triazolium dicyanamide ([MAT]-[DCA]), with and without hydrogen-capped boron nanoparticles, and the nitrogen dioxide (NO₂) oxidizer. The apparatus exploits an ultrasonic levitator enclosed within a pressure-compatible process chamber equipped with complementary Raman, ultraviolet–visible, and Fourier-transform infrared (FTIR) spectroscopic probes. Vibrational modes were first assigned to the FTIR and Raman spectra of droplets levitated in argon. Spectra were subsequently collected for pure and boron-doped [MAT][DCA] exposed to nitrogen dioxide. By comparison with electronic structure calculations, some of the newly formed modes suggest that the N atom of the NO₂ molecule bonds to a terminal N on the dicyanamide anion yielding [O₂N-NCNCN]⁻. This represents the first spectroscopic evidence of a key reaction intermediate in the oxidation of levitated ionic liquid droplets.



During the last two to three decades, ionic liquids (ILs) have received considerable attention from the organic and physical chemistry communities along with material scientists because of their role in green chemistry,^{1,2} catalysis,^{1,3,4} fuels,^{3,5–7} nuclear waste separation,^{8,9} electrochemistry,^{10,11} and pharmaceuticals.^{12,13} An ionic liquid is a liquid salt consisting of ions and ion pairs and is often defined to have a melting point below 373 K (100 °C).¹⁴ As fuels, ILs hold unique adjustable properties, such as ignition delays and energy densities, owing to the immense number of cation–anion pairs that can be customized for a specific task, for example, by changing the functional groups of the cation. Hydrazine (N₂H₄), along with its derivatives, and the oxidizer dinitrogen tetroxide in equilibrium with nitrogen dioxide (N₂O₄ ⇌ 2NO₂) is the current standard for hypergolic fuels.¹⁵ In considering the potential of ILs as greener fuels, hydrazine-based fuels have critical disadvantages, however, such as a high vapor pressure, flammability, toxicity, and a relatively low energy density.¹⁵ Energetic ionic liquids (EILs) with hypergolic properties have been synthesized as potential replacements for hydrazine as safer hypergolic fuels.^{6,16} EILs involve ions containing multiple nitrogen atoms and nitrogen–nitrogen bonds to increase the energy density;^{17,18} for example,

the formation of molecular nitrogen (N₂) from a nitrogen–nitrogen single bond (N–N) in the ionic liquid releases up to 790 kJ mol⁻¹.

To further enhance the energy density, a potential strategy is to add energetic solids such as boron to the EIL. Boron has a high gravimetric and volumetric energy density of 51 kJ g⁻¹ and 138 kJ cm⁻³ for combustion in oxygen, respectively, which is higher than that of traditional hydrocarbon fuels (35–40 kJ cm⁻³) and other combustible metals such as aluminum (84 kJ cm⁻³) or magnesium (43 kJ cm⁻³).¹⁹ However, to date, the exploitation of boron as a high-energy additive has revealed particular limitations. First, boron oxidizes upon exposure to air, creating an inert layer of boron oxide (B₂O₃) on the surface that delays the ignition. Second, in the presence of water vapor generated in the combustion, boron can become “trapped” as gaseous metaboric acid (HOBO) before forming boron oxide (B₂O₃), which hinders the release of all the available energy at temperatures between the boiling points of HOBO (1398 K) and B₂O₃ (2158 K).²⁰ Third, the combustion is a

Received: October 9, 2017

Accepted: November 28, 2017

Published: November 28, 2017

heterogeneous process limited by the diffusion to and from the surface.^{21–25} Boron nanoparticles have been proposed to mitigate the diffusion limitation by increasing the surface area to volume ratio; however, the larger surface area also increases the mass fraction of the oxide layer. Research on capping boron nanoparticles with ILs is encouraging and has been shown to prevent the formation of the oxide layer that inhibits ignition of the boron.^{23,26–28} In particular, hydrogen-terminated boron nanoparticles can be made by milling solid boron in a hydrogen atmosphere and then capping with an IL to form air-stable, unoxidized particles.²⁸

To produce the next generation of high energy-density hypersonic fuels, it is critical to unravel the mechanisms and chemical kinetics for reactions between ionic liquids and key oxidizers. In this Letter, we explore the reaction between the dicyanamide-based ionic liquid 1-methyl-4-amino-1,2,4-triazolium dicyanamide ([MAT][DCA]), with and without [MAT]-[DCA] capped, H-terminated boron nanoparticles, and nitrogen dioxide (NO₂) (Figure 1). The reactions with nitrogen

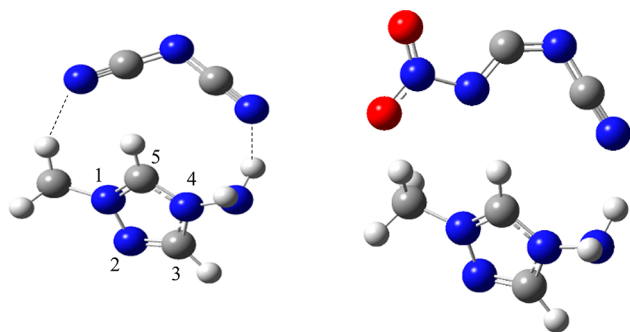


Figure 1. Structure of [MAT][DCA] (left) or [MAT][DCA] after reaction with nitrogen dioxide (NO₂) (right). The numbering convention for the positions of the atoms in the triazolium ring is shown. The relative locations of the atoms within each molecule are given in Table S4.

dioxide were performed by levitating a single droplet of the IL in an ultrasonic levitator, which is enclosed within a pressure-compatible process chamber equipped with complementary Raman, ultraviolet (UV)–visible, and Fourier-transform infrared (FTIR) spectroscopic probes (Experimental Methods in the Supporting Information).^{29–31} The levitation of a single droplet has several advantages compared to standard “bulk” experiments.^{29,30} Of particular relevance here is the unique ability for the container-less processing of a single droplet levitated in the oxidizer gas of interest at a well-defined temperature and pressure, while simultaneously probing the chemical modifications of the IL in real time and in situ.

We first consider the infrared spectra of pure [MAT][DCA] and [MAT][DCA] with 5% (by weight) of hydrogen-capped boron nanoparticles before reaction with nitrogen dioxide. A comparison of the unreacted reference spectra with measurements following reaction with the oxidizer enables the newly formed peaks to be identified. Droplets of the ionic liquid were deposited in an attenuated total reflection (ATR) accessory, and the FTIR spectra were recorded. The resulting infrared spectra are shown in Figure 2 along with fits to the individual peaks composing each spectrum. To assign vibrational modes to the peaks in the experimental spectra, the measured wavenumbers are compared with theoretical values for [MAT][DCA] and experimental data for the [DCA][−] anion

(Table S1). The assignments of the vibrational modes for [DCA][−] are based on the measured values owing to their higher accuracy and are distinguished by an asterisk. The broad underlying peaks, which are included in some spectral regions of the fits to account for the background or possibly unresolved peaks of the ionic liquid, are not assigned in Figure 2 or included in Table S1. The theoretical values were calculated by exploiting a condensed-phase generic ionic liquid (GIL) model, in which the solvation shell simulates the effects of the ionic liquid surrounding the [MAT][DCA] molecule and thus improves upon isolated gas-phase calculations (Supporting Information).^{32,33} Briefly, the peaks at 2126, 2197, and 2237 cm^{−1} are the most intense spectral features; these absorptions can be linked to the antisymmetric stretching mode $\nu_{as}(\text{C}\equiv\text{N})$, symmetric stretching mode $\nu_s(\text{C}\equiv\text{N})$, and the $\nu_s(\text{C}-\text{N}) + \nu_{as}(\text{C}-\text{N})$ combination band of the [DCA][−] anion, respectively.³⁴ In the high-wavenumber region, the absorptions in the 2970–3080 and 3140–3220 cm^{−1} ranges are attributed to C–H stretching modes of the methyl group and the triazolium ring, respectively. The N–H stretching modes of the amino group occur from 3290–3500 cm^{−1} at higher wavenumbers than for the C–H stretches. At wavenumbers between 600 and 1600 cm^{−1}, multiple overlapping peaks originate mainly from the triazolium ring and the $\nu_2^*-\nu_7^*$ modes of the [DCA][−] anion. The absorption at 2490 cm^{−1} is unique to the boron-doped sample and is attributed to the $\nu(\text{B}-\text{H})$ stretching mode.³⁵

Raman spectra of pure and boron-doped [MAT][DCA] droplets levitated in argon are shown in Figures 3 and S1, respectively, along with fits to the individual peaks composing the spectra. To assign the vibrational modes, the measured peak wavenumbers are compared with our theoretical GIL values for [MAT][DCA] and experimental data for the [DCA][−] anion (Table S2).^{34,36,37} The scattering peaks in the Raman spectra of [MAT][DCA] are similar to the absorptions in the FTIR spectra, although some differences are evident owing to the distinct selection rules for infrared and Raman spectroscopy.³⁸ For example, the ν_{13} peak at 446 cm^{−1} and the ν_{31} peak at 3507 cm^{−1} are unique to the infrared and Raman spectra, respectively. Also, the intensities of the ν_{18} , ν_3^* , ν_{23} , ν_7^* , and ν_{30} peaks relative to other peaks in the same spectrum are higher for the infrared than the Raman data; conversely, the ν_{37} and ν_{45} modes are relatively more prominent in the Raman spectrum. Furthermore, in the 2000–2300 cm^{−1} range, the relative intensities of the $\nu_6^* + \nu_7^*$, ν_8^* , and ν_9^* peaks of [DCA][−] differ significantly in the infrared and Raman spectra. In contrast to the pure [MAT][DCA] Raman spectra, the boron-doped [MAT][DCA] sample displays a structureless form which is characteristic of the Raman spectra of amorphous boron.³⁹

We next consider the oxidation of pure and boron-doped [MAT][DCA] by NO₂. After levitating the droplet in 1.3% NO₂ and 98.7% Ar, the reaction products were removed from the bottom ultrasonic-radiator plate and transferred to the ATR-FTIR spectrometer. As shown in Figure 2, the reaction between the ionic liquid and oxidizer produced many new peaks in the spectra. To identify the new absorptions, we compared fits to the nitrogen-dioxide processed spectra with the corresponding analysis for the nonoxidized ionic liquid (Figure 2). In Table 1, the fitted wavenumbers for the new peaks are compared with our theoretical GIL values for the oxidized dicyanamide anion [DCA][−],^{32,33,40} in which the nitrogen atom N of the NO₂ molecule bonds to the terminal

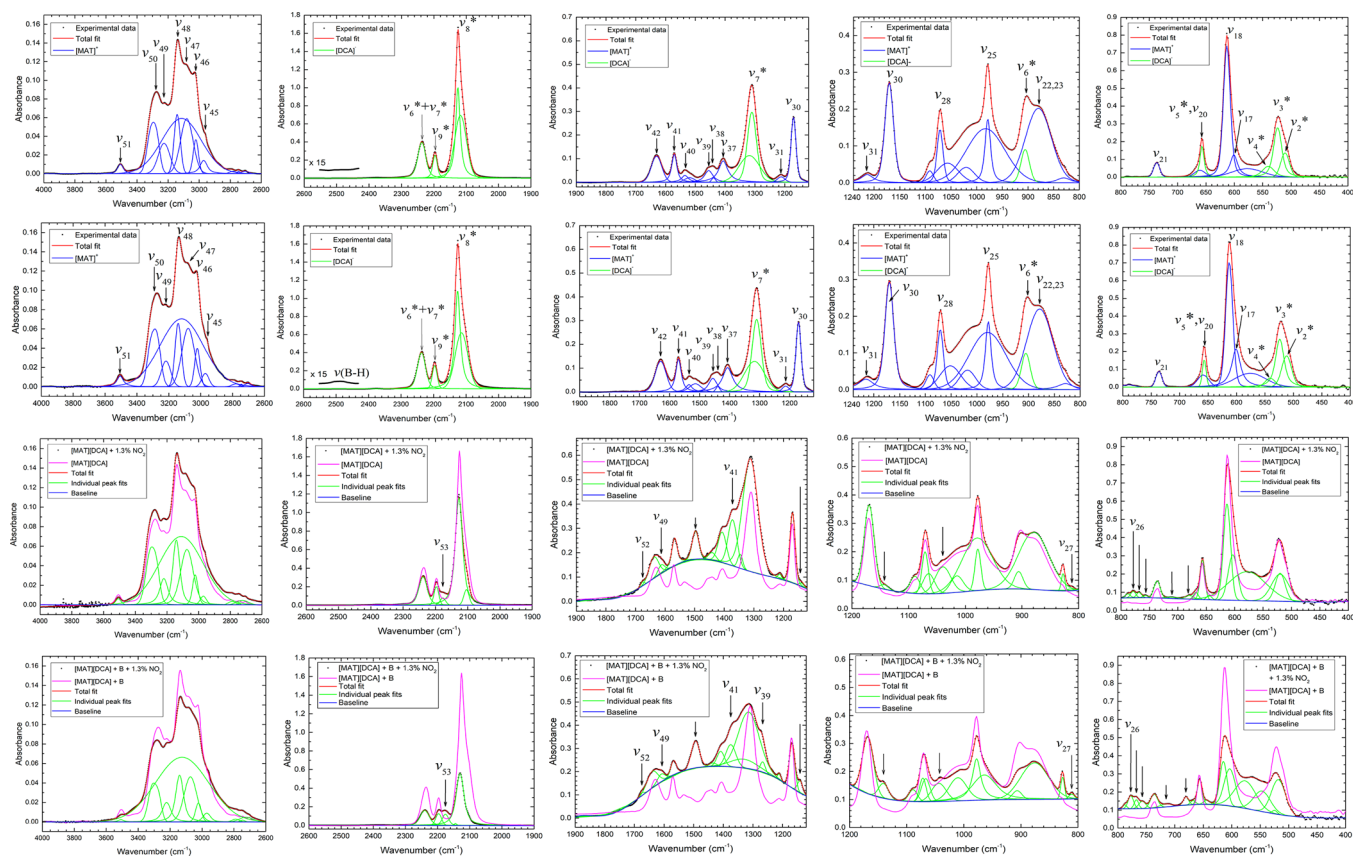


Figure 2. Top and second rows show fits to the FTIR spectra of pure and boron-doped [MAT][DCA] before reaction with nitrogen dioxide, respectively. The assignments of the vibrational modes for [DCA]⁻ are based on measured values^{34,36,37} and are distinguished by an asterisk. The remainder of the assignments were performed utilizing our theoretical GIL calculations. The third and bottom rows display fits to the FTIR spectra of pure and boron-doped [MAT][DCA], respectively, previously levitated in nitrogen dioxide and argon. The spectra of the nonreacted ionic liquids are presented for comparison purposes (purple). The newly formed vibrational peaks are identified by arrows, and the assignments are given where available.

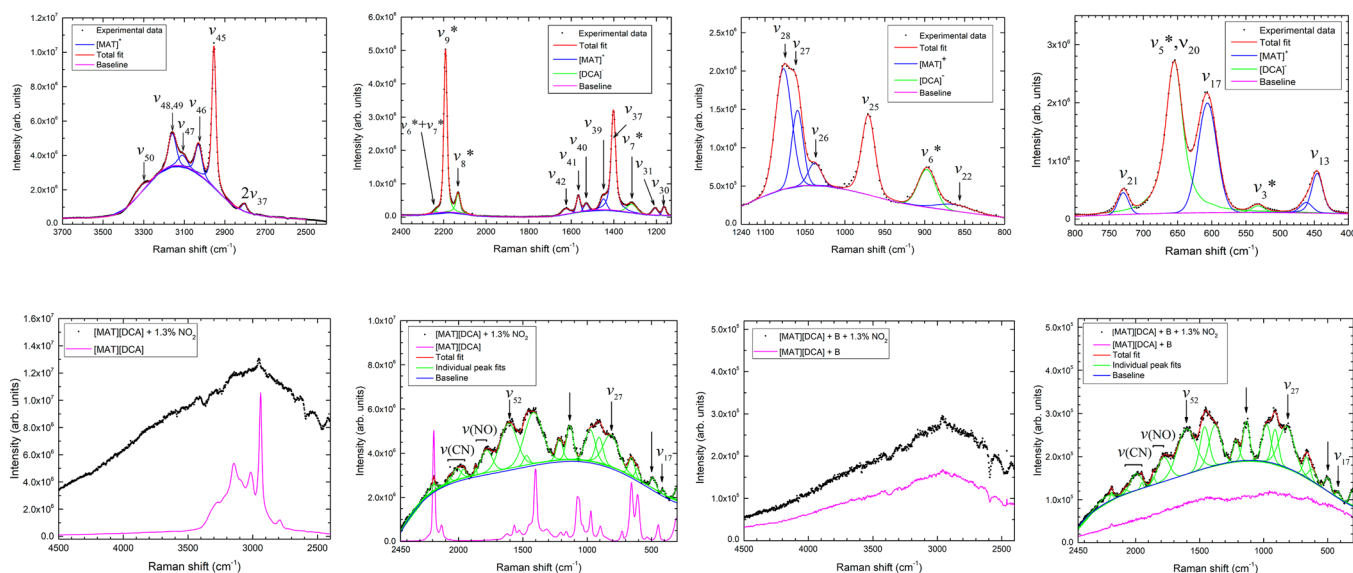


Figure 3. Top row shows fits to the Raman spectra of an [MAT][DCA] droplet levitated in argon. The assignments of the vibrational modes for [DCA]⁻ are based on measured values^{34,36,37} and are distinguished by an asterisk. The bottom row displays Raman spectra for a droplet of pure or boron-doped [MAT][DCA] levitated in nitrogen dioxide and argon. In the low Raman-shift spectra (2450–300 cm⁻¹), the individual peak fits are shown (green) and the spectra of the nonreacted [MAT][DCA] are displayed for comparison purposes (purple). The newly formed vibrational modes are identified by arrows, and the assignments are given where available.

Table 1. Wavenumbers of the New Peaks Formed in the ATR-FTIR and Raman Spectra of [MAT][DCA] or [MAT][DCA] Doped with Hydrogen-Capped Boron Nanoparticles after Reaction with Nitrogen Dioxide Assigned by Comparison with GIL Theoretical Values and also with Ref 41 for the Raman Spectra^a

		ATR-FTIR Spectra		
number	vibrational mode	theoretical wavenumbers [MAT][DCA] (cm ⁻¹)	measured wavenumbers [MAT][DCA] (cm ⁻¹)	measured wavenumbers boron-doped [MAT][DCA] (cm ⁻¹)
			680 ± 8	681 ± 1
			712 ± 2	711 ± 1
			757 ± 1	756 ± 1
			768 ± 1	768 ± 1
ν_{26}	N—NO ₂ umbrella	779	778 ± 1	778 ± 1
ν_{27}	N=C=N—NO ₂ bend + N—NO ₂ umbrella	784	815 ± 1	811 ± 1
			827 ± 1	827 ± 1
			1040 ± 3	1044 ± 3
			1143 ± 1	1141 ± 1
ν_{39}	C=N—NO ₂ stretch	1271	—	1267 ± 1
ν_{41}	N=C=N—NO ₂ symmetric stretch + NH ₂ rock	1351	1373 ± 2	1375 ± 1
			1497 ± 1	1494 ± 1
ν_{49}	O=N=O antisymmetric stretch	1568	1613 ± 7	1610 ± 1
ν_{52}	O ₂ N—NC=NCN stretch	1632	1677 ± 2	1677 ± 1
ν_{53}	N—C≡N antisymmetric stretch	2256	2177 ± 2	2176 ± 1
		Raman Spectra		
number	vibrational mode	theoretical wavenumber [MAT][DCA] (cm ⁻¹)	measured wavenumber [MAT][DCA] (cm ⁻¹)	measured wavenumber boron-doped [MAT][DCA] (cm ⁻¹)
ν_{17}	O ₂ NN=C=N in-plane bend + N—C≡N bend	432	409 ± 2	418 ± 2
			487 ± 2	498 ± 2
ν_{27}	N=C=N—NO ₂ bend + N—NO ₂ umbrella	784	813 ± 4	818 ± 2
			1135 ± 1	1136 ± 1
ν_{52}	O ₂ N—NC=NCN stretch	1632	1611 ± 2	1603 ± 1
$\nu(\text{NO})$	NO stretch	1798 ^a	1782 ± 2	1782 ± 2
$\nu(\text{NO})$	NO stretch	1837 ^a	1868 ± 1	1863 ± 2
$\nu(\text{CN})$	CN stretch	1967 ^a	1960 ± 10	1951 ± 2
$\nu(\text{CN})$	CN stretch	1998 ^a	2010 ± 20	1998 ± 3
$\nu(\text{CN})$	CN stretch	2086 ^a	2071 ± 5	2082 ± 4

^aThe quoted errors combine the uncertainties from determining the peak wavenumbers in the fitting procedure and calibrating the wavenumber scale.

N on the dicyanamide anion to form [O₂N-NCNCN]⁻ (Figure 1). The theoretical wavenumbers and vibrational assignments for the 60 fundamental modes of the molecule so formed are compiled in Table S3. Importantly, several of the new peaks correspond to vibrational modes involving the =C=N—NO₂ moiety, which suggests that NO₂ bonds to the end of the [DCA]⁻ anion. As further evidence for the proposed reaction mechanism, the peaks corresponding to the ν_8^* and ν_9^* fundamentals and $\nu_6^* + \nu_7^*$ combination band of the [DCA]⁻ anion between 2100 and 2300 cm⁻¹ have decreased because of loss of the anion in the reaction with nitrogen dioxide. However, the infrared spectra also display new peaks not predicted by the present theoretical calculations at 680, 712, 757, 768, 827, 1040, 1143, and 1497 cm⁻¹ in the oxidized [MAT][DCA] and at similar wavenumbers for the oxidized, boron-doped [MAT][DCA] spectra (Table 1). Our calculations show that the NO₂ molecule does not bond to the central N atom of the [DCA]⁻ anion but moves away to form a

nonbonded complex. Therefore, the bonding of NO₂ to the central N atom cannot explain the appearance of the new peaks in the spectra. In contrast, the theoretical model shows that the nitrogen atom of the NO₂ molecule can bond to a carbon atom in [DCA]⁻, and the resulting nine additional vibrational modes could account for many of the unassigned new peaks in Table 1. The molecular dynamics simulations for [MAT][DCA] reactions with nitrogen dioxide required to better understand the formation of the new peaks are currently underway and will be published. Regarding the effects of the boron, the oxidizer produced essentially the same new peaks for the [MAT][DCA] with and without boron nanoparticles; therefore, the newly emerging peaks in the boron-doped samples can also be linked to the reaction of the nitrogen dioxide molecule with the [DCA]⁻ anion forming [O₂N-NCNCN]⁻ (Figure 1) rather than to an initial reaction of nitrogen dioxide with the boron-based nanoparticles. The absence of clear evidence for the formation of new peaks involving boron is consistent with the

[MAT][DCA] capping limiting the oxidation of the nanoparticles.

The corresponding in situ Raman spectra and individual peak fits for an [MAT][DCA] droplet, with and without [MAT]-[DCA] capped, hydrogenated boron nanoparticles, and levitated in the same NO_2 and Ar gas mixture are shown in Figure 3. The bottom curves within each figure (purple lines) are the spectra before reaction, whereas the top curves (black dots) show the final spectral forms reached after full reaction with the oxidizer gas. In the low Raman-shift region from 2450 to 300 cm^{-1} , the nitrogen dioxide causes the amplitude of the sharp peaks from the unreacted [MAT][DCA] to reduce and be replaced by several large, broad new features at different wavenumbers. As for the FTIR data, the Raman spectra of pure and boron-doped [MAT][DCA] following oxidation are essentially the same, which confirms that the new peaks in the boron-doped sample involve reaction of the nitrogen dioxide molecule with the $[\text{DCA}]^-$ anion rather than the boron nanoparticles. When interpreting the spectra, it is necessary to distinguish between the newly formed peaks and the structure remaining from the unreacted [MAT][DCA]. By comparison with our theoretical GIL calculations, in Table 1 we assign vibrational modes to the newly formed peaks. The peaks at 409, 813, and 1611 cm^{-1} can be associated with vibrational modes of the $=\text{C}=\text{N}-\text{NO}_2$ moiety, which supports our contention that NO_2 bonds to one of the ends of the $[\text{DCA}]^-$ anion. The new peaks in the range from 1780 to 2070 cm^{-1} cannot be linked to $[\text{O}_2\text{N}-\text{NCNCN}]^-$ and so are attributed to the $\nu(\text{NO})$ and $\nu(\text{CN})$ stretching modes of the $\text{N}-\text{O}-\text{C}-\text{N}$ and $\text{C}-\text{N}-\text{N}-\text{O}$ functional groups.⁴¹ Further studies are required to better understand the cause of the new structure in the 1780 – 2070 cm^{-1} region. By determining the decrease in the area of the $[\text{DCA}]^-$ anion peaks versus time, we deduced that the time constant ($1/e$) for the reaction is 16 ± 4 min when the concentration was 1.3% NO_2 . The relatively slow reaction rate confirms that, in contrast to nitric acid (HNO_3), dicyanamide-based ionic liquids are not hypergolic with NO_2 or N_2O_4 . Furthermore, the reaction rate was significantly reduced as a result of diluting the oxidizer in argon.

Finally, the UV–visible spectra of pure and boron-doped [MAT][DCA] droplets in the 200 – 1100 nm wavelength range are explored. We first discuss the results before reaction with the nitrogen dioxide. For [MAT][DCA], as shown in Figure 4, the spectrum reveals a minimum in the reflectance, and hence a maximum in the absorption, across the 230 – 380 nm region. Time-dependent density functional theory (TD-DFT) calculations at the M06/6-31+G(d,p) level suggest that this

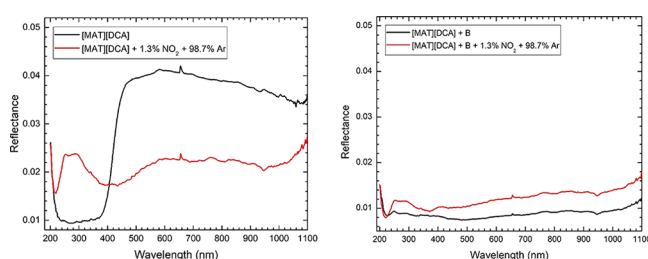


Figure 4. UV–visible spectra for a droplet of [MAT][DCA] (left) or [MAT][DCA] doped with hydrogen-capped boron nanoparticles (right). The reference spectra (black lines) were collected prior to the reaction; the spectra in red were collected after reaction with the nitrogen dioxide.

absorption feature originates from $\pi \rightarrow \pi^*$ transitions in [MAT][DCA] (Supporting Information). The addition of the boron nanoparticles causes the ionic liquid to blacken, and consequently the region of high absorption (or low reflectance) extends across the full spectral range. The absorption of boron in the 200 – 1100 nm region is produced by interband transitions.^{42,43} Also shown in Figure 4 are the UV–visible spectra after reaction with the oxidizer. The spectrum of oxidized [MAT][DCA] developed a sharp absorption peak at around 220 nm succeeded by a broad absorption feature from 300 – 600 nm , which is similar to the absorption spectrum of nitrogen dioxide in the 200 – 700 nm range⁴⁴ and thus suggests that some of the features are produced by nitrogen dioxide dissolved in the droplet. The [MAT][DCA] spectrum appears to reduce significantly to be replaced by the nitrogen dioxide absorption, which implies that the oxidizer has a relatively high concentration at least near the surface of the droplet. It was previously reported that nitric acid (HNO_3) tends to stay on the surface of IL droplets owing to repulsion by the highly polar ionic liquid;⁴⁵ therefore, a high concentration of nitrogen dioxide in the surface region might be expected here.

In summary, we investigated the initial steps in the oxidation of levitated droplets of [MAT][DCA] and [MAT][DCA] doped with IL-capped, hydrogen-terminated boron nanoparticles by nitrogen dioxide (NO_2) in an argon atmosphere. The Raman and infrared spectra of the samples were assigned with the help of theoretical calculations exploiting a condensed-phase GIL model at the M06/6-31+G(d,p) level of theory. Some of the newly emerged peaks suggest that the reaction is initiated by the nitrogen atom of the nitrogen dioxide (NO_2) molecule bonding to one of the terminal nitrogen atoms of the $[\text{DCA}]^-$ anion yielding a $[\text{O}_2\text{N}-\text{NCNCN}]^-$ species. In support of our suggested reaction mechanism, the intensities of the $[\text{DCA}]^-$ stretching modes reduced significantly. The absence of clear evidence for the formation of new peaks involving boron is consistent with the [MAT][DCA] capping limiting the oxidation of the nanoparticles. Further theoretical studies are required to better understand the formation of the new peaks unassigned by the present model. This work provides a template of how to search for hitherto elusive reaction intermediates in the oxidation of ionic liquids.

EXPERIMENTAL METHODS

See the Supporting Information.

ASSOCIATED CONTENT

Supporting Information

The Supporting Information is available free of charge on the ACS Publications website at DOI: 10.1021/acs.jpcllett.7b02669.

Experimental methods; computational methods; Figure S1 and Tables S1–S4 as described in the text (PDF)

AUTHOR INFORMATION

Corresponding Author

*E-mail: ralfk@hawaii.edu.

ORCID

Ghanshyam L. Vaghjiani: 0000-0001-7473-7388

Scott L. Anderson: 0000-0001-9985-8178

Ralf I. Kaiser: 0000-0002-7233-7206

Notes

The authors declare no competing financial interest.

ACKNOWLEDGMENTS

This work was supported by the Office of Naval Research under Grant N00014-16-1-2078 (Hawaii) and by the Air Force Research Laboratory in Space Propulsion (RQRS) and Propellants (RQRP) Branches at Edwards Air Force Base. Particle production was supported by the Office of Naval Research under Grant N00014-15-1-2681 (Utah).

REFERENCES

- (1) Dai, C.; Zhang, J.; Huang, C.; Lei, Z. Ionic Liquids in Selective Oxidation: Catalysts and Solvents. *Chem. Rev.* **2017**, *117*, 6929–6983.
- (2) Earle, M. J.; Seddon, K. R. Ionic liquids. Green Solvents for the Future. *Pure Appl. Chem.* **2000**, *72*, 1391–1398.
- (3) Zhang, Z.; Song, J.; Han, B. Catalytic Transformation of Lignocellulose into Chemicals and Fuel Products in Ionic Liquids. *Chem. Rev.* **2017**, *117*, 6834–6880.
- (4) Parvulescu, V. I.; Hardacre, C. Catalysis in Ionic Liquids. *Chem. Rev.* **2007**, *107*, 2615–2665.
- (5) Watanabe, M.; Thomas, M. L.; Zhang, S.; Ueno, K.; Yasuda, T.; Dokko, K. Application of Ionic Liquids to Energy Storage and Conversion Materials and Devices. *Chem. Rev.* **2017**, *117*, 7190–7239.
- (6) Zhang, Y.; Gao, H.; Joo, Y.-H.; Shreeve, J. M. Ionic Liquids as Hypergolic Fuels. *Angew. Chem., Int. Ed.* **2011**, *50*, 9554–9562.
- (7) Sebastiao, E.; Cook, C.; Hu, A.; Murugesu, M. Recent Developments in the Field of Energetic Ionic Liquids. *J. Mater. Chem. A* **2014**, *2*, 8153–8173.
- (8) Ventura, S. P. M.; e Silva, F. A.; Quental, M. V.; Mondal, D.; Freire, M. G.; Coutinho, J. A. P. Ionic-Liquid-Mediated Extraction and Separation Processes for Bioactive Compounds: Past, Present, and Future Trends. *Chem. Rev.* **2017**, *117*, 6984–7052.
- (9) Cocalia, V. A.; Jensen, M. P.; Holbrey, J. D.; Spear, S. K.; Stepiński, D. C.; Rogers, R. D. Identical Extraction Behavior and Coordination of Trivalent or Hexavalent f-Element Cations Using Ionic Liquid and Molecular Solvents. *Dalton Trans.* **2005**, 1966–1971.
- (10) Lin, M.-C.; Gong, M.; Lu, B.; Wu, Y.; Wang, D.-Y.; Guan, M.; Angell, M.; Chen, C.; Yang, J.; Hwang, B.-J.; Dai, H. An Ultrafast Rechargeable Aluminum-Ion Battery. *Nature* **2015**, *520*, 324–328.
- (11) MacFarlane, D. R.; Tachikawa, N.; Forsyth, M.; Pringle, J. M.; Howlett, P. C.; Elliott, G. D.; Davis, J. H.; Watanabe, M.; Simon, P.; Angell, C. A. Energy Applications of Ionic Liquids. *Energy Environ. Sci.* **2014**, *7*, 232–250.
- (12) Egorova, K. S.; Gordeev, E. G.; Ananikov, V. P. Biological Activity of Ionic Liquids and Their Application in Pharmaceuticals and Medicine. *Chem. Rev.* **2017**, *117*, 7132–7189.
- (13) Zakrewsky, M.; Lovejoy, K. S.; Kern, T. L.; Miller, T. E.; Le, V.; Nagy, A.; Goumas, A. M.; Iyer, R. S.; Del Sesto, R. E.; Koppisch, A. T.; Fox, D. T.; Mitragotri, S. Ionic Liquids as a Class of Materials for Transdermal Delivery and Pathogen Neutralization. *Proc. Natl. Acad. Sci. U. S. A.* **2014**, *111*, 13313–13318.
- (14) Lei, Z.; Chen, B.; Koo, Y.-M.; MacFarlane, D. R. Introduction: Ionic Liquids. *Chem. Rev.* **2017**, *117*, 6633–6635.
- (15) Clark, J. D. *Ignition! An Informal History of Liquid Rocket Propellants*; Rutgers University Press: New Brunswick, NJ, 1972.
- (16) Zhang, Y.; Shreeve, J. M. Dicyanoborate-Based Ionic Liquids as Hypergolic Fluids. *Angew. Chem., Int. Ed.* **2011**, *50*, 935–937.
- (17) Politzer, P.; Murray, J. S.; Seminario, J. M.; Lane, P.; Edward Grice, M.; Concha, M. C. Computational Characterization of Energetic Materials. *J. Mol. Struct.: THEOCHEM* **2001**, *573*, 1–10.
- (18) Rice, B. M.; Pai, S. V.; Hare, J. Predicting Heats of Formation of Energetic Materials using Quantum Mechanical Calculations. *Combust. Flame* **1999**, *118*, 445–458.
- (19) Cox, J. D.; Wagman, D. D.; Medvedev, V. A. *CODATA Key Values for Thermodynamics*; Hemisphere Publishing Corp.: New York, 1989.
- (20) Ulas, A.; Kuo, K. K.; Gotzmer, C. Ignition and Combustion of Boron Particles in Fluorine-Containing Environments. *Combust. Flame* **2001**, *127*, 1935–1957.
- (21) Antaki, P.; Williams, F. A. Observations on the Combustion of Boron Slurry Droplets in Air. *Combust. Flame* **1987**, *67*, 1–8.
- (22) King, M. K. Ignition and Combustion of Boron Particles and Clouds. *J. Spacecr. Rockets* **1982**, *19*, 294–306.
- (23) Van Devener, B.; Perez, J. P. L.; Jankovich, J.; Anderson, S. L. Oxide-Free, Catalyst-Coated, Fuel-Soluble, Air-Stable Boron Nanopowder as Combined Combustion Catalyst and High Energy Density Fuel. *Energy Fuels* **2009**, *23*, 6111–6120.
- (24) Young, G.; Sullivan, K.; Zachariah, M. R.; Yu, K. Combustion Characteristics of Boron Nanoparticles. *Combust. Flame* **2009**, *156*, 322–333.
- (25) Zhou, W.; Yetter, R. A.; Dryer, F. L.; Rabitz, H.; Brown, R. C.; Kolb, C. E. Multi-Phase Model for Ignition and Combustion of Boron Particles. *Combust. Flame* **1999**, *117*, 227–243.
- (26) Perez, J. P. L.; McMahan, B. W.; Schneider, S.; Boatz, J. A.; Hawkins, T. W.; McCrary, P. D.; Beasley, P. A.; Kelley, S. P.; Rogers, R. D.; Anderson, S. L. Exploring the Structure of Nitrogen-Rich Ionic Liquids and Their Binding to the Surface of Oxide-Free Boron Nanoparticles. *J. Phys. Chem. C* **2013**, *117*, 5693–5707.
- (27) Perez, J. P. L.; McMahan, B. W.; Anderson, S. L. Functionalization and Passivation of Boron Nanoparticles with a Hypergolic Ionic Liquid. *J. Propul. Power* **2013**, *29*, 489–495.
- (28) Perez, J. P. L.; Yu, J.; Sheppard, A. J.; Chambreau, S. D.; Vaghjiani, G. L.; Anderson, S. L. Binding of Alkenes and Ionic Liquids to B-H-Functionalized Boron Nanoparticles: Creation of Particles with Controlled Dispersibility and Minimal Surface Oxidation. *ACS Appl. Mater. Interfaces* **2015**, *7*, 9991–10003.
- (29) Brotton, S. J.; Kaiser, R. I. Novel High-Temperature and Pressure-Compatible Ultrasonic Levitator Apparatus Coupled to Raman and Fourier Transform Infrared Spectrometers. *Rev. Sci. Instrum.* **2013**, *84*, 055114.
- (30) Brotton, S. J.; Kaiser, R. I. In Situ Raman Spectroscopic Study of Gypsum ($\text{CaSO}_4 \cdot 2\text{H}_2\text{O}$) and Epsomite ($\text{MgSO}_4 \cdot 7\text{H}_2\text{O}$) Dehydration Utilizing an Ultrasonic Levitator. *J. Phys. Chem. Lett.* **2013**, *4*, 669–673.
- (31) Bennett, C. J.; Brotton, S. J.; Jones, B. M.; Misra, A. K.; Sharma, S. K.; Kaiser, R. I. High-Sensitivity Raman Spectrometer To Study Pristine and Irradiated Interstellar Ice Analogs. *Anal. Chem.* **2013**, *85*, 5659–5665.
- (32) Marenich, A. V.; Cramer, C. J.; Truhlar, D. G. Universal Solvation Model Based on Solute Electron Density and on a Continuum Model of the Solvent Defined by the Bulk Dielectric Constant and Atomic Surface Tensions. *J. Phys. Chem. B* **2009**, *113*, 6378–6396.
- (33) Bernales, V. S.; Marenich, A. V.; Contreras, R.; Cramer, C. J.; Truhlar, D. G. Quantum Mechanical Continuum Solvation Models for Ionic Liquids. *J. Phys. Chem. B* **2012**, *116*, 9122–9129.
- (34) Reckeweg, O.; DiSalvo, F. J.; Schulz, A.; Blaschkowski, B.; Jagiella, S.; Schleid, T. Synthesis, Crystal Structure, and Vibrational Spectra of the Anhydrous Lithium Dicyanamide $\text{LiN}(\text{CN})_2$. *Z. Anorg. Allg. Chem.* **2014**, *640*, 851–855.
- (35) Socrates, G. *Infrared and Raman Characteristic Group Frequencies: Tables and Charts*, 3rd ed.; Wiley: Chichester, U.K., 2001.
- (36) Paschoal, V. H.; Faria, L. F. O.; Ribeiro, M. C. C. Vibrational Spectroscopy of Ionic Liquids. *Chem. Rev.* **2017**, *117*, 7053–7112.
- (37) Kiefer, J.; Noack, K.; Penna, T. C.; Ribeiro, M. C. C.; Weber, H.; Kirchner, B. Vibrational Signatures of Anionic Cyano Groups in Imidazolium Ionic Liquids. *Vib. Spectrosc.* **2017**, *91*, 141–146.
- (38) Colthup, N. B.; Daly, L. H.; Wiberley, S. E. *Introduction to Infrared and Raman Spectroscopy*, 3rd ed.; Academic Press: Boston, 1990.
- (39) Parakhonskiy, G.; Dubrovinskaia, N.; Bykova, E.; Wirth, R.; Dubrovinsky, L. Experimental Pressure-Temperature Phase Diagram of Boron: Resolving the Long-Standing Enigma. *Sci. Rep.* **2011**, *1*, 96.
- (40) Zhao, Y.; Truhlar, D. G. The M06 Suite of Density Functionals for Main Group Thermochemistry, Thermochemical Kinetics, Non-covalent Interactions, Excited States, and Transition Elements: Two New Functionals and Systematic Testing of Four M06-Class

Functionals and 12 Other Functionals. *Theor. Chem. Acc.* **2008**, *120*, 215–241.

(41) Maier, G.; Reisenauer, H. P.; Eckwert, J.; Naumann, M.; DeMarco, M. Isomers of the Elemental Composition CN_2O . *Angew. Chem., Int. Ed. Engl.* **1997**, *36*, 1707–1709.

(42) Kuhlmann, U.; Werheit, H.; Lundstrom, T.; Robers, W. Optical Properties of Amorphous Boron. *J. Phys. Chem. Solids* **1994**, *55*, 579–587.

(43) Werheit, H.; Schmechel, R. The Complete Optical Spectrum of Beta-Rhombohedral Boron. *J. Solid State Chem.* **1997**, *133*, 129–131.

(44) Schneider, W.; Moortgat, G. K.; Tyndall, G. S.; Burrows, J. P. Absorption Cross-Sections of NO_2 in the UV and Visible Region (200 - 700 nm) at 298 K. *J. Photochem. Photobiol., A* **1987**, *40*, 195–217.

(45) Chambreau, S. D.; Koh, C. J.; Popolan-Vaida, D. M.; Gallegos, C. J.; Hooper, J. B.; Bedrov, D.; Vaghjiani, G. L.; Leone, S. R. Flow-Tube Investigations of Hypergolic Reactions of a Dicyanamide Ionic Liquid Via Tunable Vacuum Ultraviolet Aerosol Mass Spectrometry. *J. Phys. Chem. A* **2016**, *120*, 8011–8023.